Journal of Applied Mechanics and Technical Physics, Vol. 43, No. 6, pp. 867–876, 2002

EXPERIMENTAL AND NUMERICAL STUDY OF A HYPERSONIC SEPARATED FLOW IN THE VICINITY OF A CONE-FLARE MODEL

I. A. Bedarev, A. A. Maslov, A. A. Sidorenko, N. N. Fedorova, and A. N. Shiplyuk

UDC 532.517.4 : 533.601.155

An axisymmetric laminar separated flow in the vicinity of a cone-flare model is studied experimentally and numerically for a Mach number $M = 6$. The distributions of pressure and Stanton numbers along the model surface and velocity profiles in the region of shock wave–boundary layer interaction are measured and compared with the calculated data. The influence of the laminar–turbulent transition on flow parameters is studied numerically.

Introduction. In a supersonic flow around aircraft elements, shock waves and expansion waves interact with the boundary layer on the aircraft surface. Strong interactions (strong shock waves and high Mach numbers) generate extensive separated regions, which significantly reconstruct the wave pattern of the flow and change dynamic and heat loads. For aircraft design and optimization, it is important to exactly determine flow parameters at the points of flow separation and reattachment, since surface loads here are most intense. The separation-point position is known to be determined to a large extent by the boundary-layer state upstream of the interaction region. Since shear stresses on the wall counteracting with the adverse pressure gradient in turbulent boundary layers are significantly higher than in the laminar flow, separation of a turbulent boundary layer occurs at higher pressure gradients. At the same time, the turbulent boundary layer involves higher heat fluxes and skin friction. In the cases considered, the separation-region structure can be significantly different. For instance, the presence of secondary separation regions leads to additional heat and aerodynamic loads. Hence, it is important to take into account the boundary-layer state upstream of the zone of interaction and laminar–turbulent transition in supersonic boundary layers to reliably predict aerodynamic loads and heat fluxes.

The properties of laminar and turbulent separations in supersonic flows have been considered in many experimental and numerical studies (see, e.g., reviews [1–4]. As was noted in [5], the adequacy of mathematical simulation of laminar separated flows is mainly determined by the method of approximation and computer performance. In the case of turbulent flows, an additional factor is the method of turbulence modeling. However, in an actual flow, it is often impossible to determine the boundary-layer state exactly, since the laminar–turbulent transition occurs in the interaction region. Depending on conditions of a particular experiment, the transition region can be located in the vicinity of the separated or reattachment shock. Apparently, this is related to the increase in fluctuations on shock waves (both inside the boundary layer and in the external inviscid region), which accelerates the laminar–turbulent transition process. The presence of transition inside the interaction region leads to redistribution of parameters on the model surface.

The paper of Chapman et al. [6] is one of the first works where the influence of the laminar–turbulent transition on separated flow parameters was studied experimentally. The results of this work are described in detail in [7]. The main differences between the laminar, turbulent, and transitional regimes of the flow around backward- and forward-facing steps, which were noted in [6], are caused by the separation-region length and by the level of

Institute of Theoretical and Applied Mechanics, Siberian Division, Russian Academy of Sciences, Novosibirsk 630090. Translated from Prikladnaya Mekhanika i Tekhnicheskaya Fizika, Vol. 43, No. 6, pp. 100–112, November–December, 2002. Original article submitted April 29, 2002.

0021-8944/02/4306-0867 $27.00 © 2002 Plenum Publishing Corporation

relative pressure in the separation region. In the laminar case, the separation-region length is considerably greater, which is evidenced by the extended pressure plateau; the level of pressure in the plateau region is not very high. An increase in the Reynolds number led to a decrease in pressure in the plateau region. In the case of transitional separation, the transition point was located between the separation and reattachment points, which was the reason for unsteadiness of the process. In the transitional regime, the flow characteristics were significantly dependent on the Reynolds number, and the separation-region length decreased with increasing Reynolds number. In the case of a fully turbulent flow, where the transition occurred significantly upstream of the flow-separation point, the separation-region length was significantly smaller, and the pressure in the plateau region was higher. In this case, a change in the Reynolds number exerted no significant effect on the pressure distribution over the model surface, except for the region behind the reattachment point where the pressure tended to a value determined by the inviscid solution with increasing Reynolds number. By introducing new self-similar variables, Chapman et al. [6] managed to eliminate almost completely the effect of the Reynolds number and flow geometry on the dependence of pressure on the distance and Mach number and to explain the correlations obtained on the basis of the free-interaction theory.

It is noted in the review [8] that the separation region often acts as a source of hydrodynamic instability, which is manifested at low Reynolds numbers and can initiate the laminar–turbulent transition in the mixing layer above the separation bubble. A change in external conditions, in turn, affects the emergence of separation and can alter the separation-region length and other properties.

Hammond and Redekopp [9] considered velocity profiles near the separation region of an incompressible boundary layer from the viewpoint of linear stability. Inflection points typical of velocity profiles in the separation region are responsible for the linearly unstable mode. If the maximum velocity of the reverse flow reaches 30% of the external flow velocity, the flow becomes absolutely unstable, and the process becomes unsteady.

Results of experimental and numerical studies of supersonic separated flows for various configurations and flow parameters for which the transitional phenomena play an important role are reported in [10–18]. Thus, Wright et al. [10] compared the experimental and calculated flow characteristics in the vicinity of a double cone for $M = 8$ and different cone angles. In one of the cases considered, which corresponds to an interaction of type V in the classification of Edney [19], the separation-region length in experimental and numerical data was significantly different. In addition, the calculations performed for a laminar flow did not agree with the experimental dependence of the separation-region length on the Reynolds number. The assumption on the turbulent character of the flow in the interaction region and the use of the two-parameter k–ε turbulence model made it possible to significantly improve the accuracy of determining the separation-region length and to describe qualitatively the flow parameters as functions of the Reynolds number.

A similar geometric configuration was examined in [11], where special attention was paid to the influence of the angle of attack and forebody bluntness on the flow structure and heat transfer. The experiments were performed for $M = 10$ for five angles of attack from 0 to 35°. The numerical calculations were performed using two- and three-dimensional codes. The calculations for the turbulent boundary layer were conducted using the algebraic Baldwin–Lomax model. A comparison of calculation results obtained using different codes showed that good agreement with experimental data on heat transfer at high angles of attack can be reached by taking into account the influence of three-dimensional effects and transitional phenomena.

Filippis et al. [12] compared experimental and numerical results of studying the flow in the vicinity of the Hermes-type reentry vehicle for $M = 10$. The objective of [12] was to study the heat-transfer intensity for various angles of elevon deflection and also to evaluate the effect of the laminar–turbulent transition location on flow parameters. The calculations were performed using an algebraic turbulence model and two-parameter two-layer turbulence model of the k–ε type. An intermittency function was introduced to simulate the transition in a given range of the streamwise coordinate. In the case of the minimum elevon-deflection angle, the numerical data were compared to the empirical dependence of relative heat transfer on relative pressure. The allowance for the transitional character of the flow in calculations with the differential model of turbulence improves the accuracy of heat-flux determination.

Nance et al. [13] reported the calculation results for a wake flow behind a bluff body, such as a spherically blunted 70-degree cone for $M = 6$. An analysis of numerous experimental data shows that a drastic increase in heat transfer occurs behind the reattachment point, which is caused by the laminar–turbulent transition in the shear layer. The work was aimed at evaluating the applicability of turbulence models for simulating the transition in the situation described. The transition was simulated using the k–ζ and k–ω models of turbulence [20, 21] with

an intermittency function. Several cases were considered, with the transition-point location being fixed at different parts of the test model. Comparisons with available experimental data revealed advantages of the k–ζ turbulence model and the importance of a proper choice of the transition-point location.

The flow around a 70-degree sphere–cone planetary entry vehicle model was studied in [14] experimentally and numerically for M = 10 and Reynolds numbers based on the maximum model diameter $\mathrm{Re}_D = 8.23{\cdot}10^4$–$3.15{\cdot}10^5$. Heat fluxes along the model surface were measured, and calculations within the framework of two-dimensional axisymmetric Navier–Stokes equations were performed. The calculated and experimental data were in good agreement on the forebody and afterbody of the vehicle and also on the sting surface upstream of the reattachment point for all Reynolds numbers examined. The numerical and experimental data are significantly different, however, behind the reattachment point, and the difference increases with increasing Reynolds number. To explain this phenomenon, a hypothesis of the laminar–turbulent transition in the vicinity of the shear-layer reattachment point was put forward, but no calculations were presented to support this hypothesis.

Laurien [15] performed a numerical study of the laminar–turbulent transition on a reentry vehicle that was a spherically blunted 9-degree cone. The calculation was performed within the framework of Navier–Stokes equations for M = 27, $\mathrm{Re}_D = 21 \cdot 10^3$ and M = 5, $\mathrm{Re}_D = 9 \cdot 10^6$. After determining all flow parameters, a linear analysis of stability of the numerical solution was performed, which revealed that the solutions are linearly stable in both cases considered. Nevertheless, this result contradicted the experimental data on the turbulent flow character at M = 5, which necessitated a numerical analysis of nonlinear stability. The results of direct numerical simulation showed that, in the case of M = 5 and $\mathrm{Re}_D = 9 \cdot 10^6$, finite-amplitude perturbations increased, which resulted in the appearance of turbulent spots. Thus, it was demonstrated that numerical simulation allows one to obtain information on transitional phenomena even in the case of linearly stable flows, where the e^N method cannot be used to determine the transition point.

Results of numerical simulation of transitional flows past a flat plate and a cylinder with the use of the q–ω model of turbulence [22] were reported in [16–18]. It was stated that this model could describe the transition with an acceptable accuracy without introducing any intermittency functions. Parametric calculations of the transition on a flat plate [16] show that the transition location depends on the Mach number and turbulent kinetic energy in the external flow. The calculations of the flow around a cylinder with an isothermal wall for M = 5 and $\mathrm{Re}_D = 10^4$–10^8 revealed that flow turbulization leads to a downstream shift of the separation point and to an increase in the relative heat flux at the rear stagnation point.

The review of available data shows that the problem under study is of significant interest from the viewpoint of both explaining physical features of the complex flow and developing the methodology of modeling the laminar–turbulent transition and studying its effect on flow parameters.

1. Test Conditions. The experiments were performed in a T-326 hypersonic wind tunnel of the Institute of Theoretical and Applied Mechanics of the Siberian Division of the Russian Academy of Sciences for a free-stream Mach number $\mathrm{M}_\infty = 5.92$. The T-326 wind tunnel [23] is an ejector-type facility with atmospheric exhaustion (the time of continuous operation is determined by the operation regime and reaches 20 min for $\mathrm{M}_\infty \approx 6$). The test section is the Eiffel chamber; the flow-core diameter is 180 mm. To avoid condensation, the air was heated by an electric heater. The nonuniformity of the velocity field in the flow was lower than 0.7% for $\mathrm{M}_\infty \approx 6$. The pressure and temperature in the plenum chamber were sustained constant within 0.5%. The level of mass-flow fluctuations under our test conditions ($\mathrm{M}_\infty = 5.92$, $T_0 = 390$ K, $P_0 = 1.01$ MPa, and $\mathrm{Re}_1 = 12.5 \cdot 10^6$ m^{-1}) was approximately 1%, which is typical of conventional wind tunnels.

The experimental model shown schematically in Fig. 1 was a composite cone. The model was mounted along the nozzle centerline at zero incidence and sideslip angles. The error of model mounting was determined by pressure measurements on the surface at diametrically opposite points and reached 0.06°. The bluntness radius of the model nose was less than 0.01 mm. The model surface had 30 pressure taps located with allowance for the expected size and position of the separation region. The pressure taps near the model-contour inflection were located with a step of 1.5 mm in the longitudinal direction. In addition, the model was equipped by a thermocouple for controlling the model temperature during the tests. The measurements were performed after heating the model to reach adiabatic conditions.

The pressure on the model surface was measured by three fast-response induction gauges with a range of 0–10 kPa. By means of a scannivalve, the gauges were consecutively connected to each of the ten pressure taps allocated for this scannivalve; the pressure was measured after pressure stabilization in the pipeline. The error of pressure measurement was less than 1% of the upper limit of the gauge range.

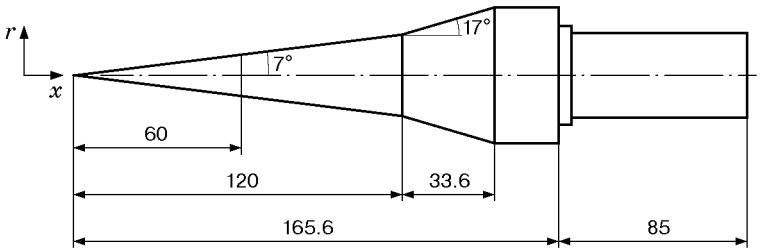

Fig. 1. Schematic of the experimental model.

The pressure distribution in the boundary layer of the model and in the separation region was obtained on the basis of the measured total pressure profiles P_0' behind the normal shock and also using a TPT-4 constant-current hot-wire anemometer. The model was turned around the longitudinal axis in a manner to eliminate possible influence of pressure taps on the boundary-layer flow. The pressure P_0' was measured by a strain gauge with a range of 0–150 kPa. The Pitot probe had a thickness of 0.25 mm and was moved across the boundary layer with a step of 0.05 mm. For this size of the probe, the measurement error was less than 3%. Since the use of a rather large Pitot probe for measurements in a thin boundary layer and separation region makes doubtful the accuracy of the measured velocity profiles, the same investigations were performed using the hot-wire anemometer. The use of probes made of tungsten wire 5 M*u*m in diameter and 1.3 mm long ensured the minimum level of perturbations introduced into the flow. The probes were moved in the boundary layer with an accuracy up to 0.01 mm, and the initial position of the probes relative to the model surface was determined by the electric contact.

Velocity was reconstructed from the measured values of P_0' using the Crocco integral. The procedure of processing hot-wire data is described in [24]. In all cases, the velocity profiles obtained by both methods almost coincide.

In the course of experiments, the values of the measured parameters (P_s, P_0', Pitot probe position, plenum-chamber parameters, and hot-wire measurements) were recorded into a personal computer. The computer controlled the motion of gauges and rotation of the model in accordance with the test program.

Heat fluxes were measured on the surface of a model of similar geometry, which was made of AG-4V fiberglass plastic. This material has a low thermal conductivity, its characteristics are well studied; therefore, it is widely used for manufacturing models for aerodynamic experiments. The model nose was made of steel to ensure a small bluntness radius. The temperature distribution on the model surface was registered by a TB-M3 infrared imager in the line-by-line scanning mode.

The experiment was performed as follows. The model at room temperature was rapidly introduced into the flow by means of a special mechanism. To increase the measurement accuracy, the experiments were performed for flow parameters $P_0 = 1.21$ MPa and $T_0 = 413$ K. The temperature distribution at 256 point on the surface along the cone generatrix was recorded during 120 sec.

The technique for heat-flux determination on the basis of wall-temperature measurements in time is based on solving one-dimensional unsteady heat-conduction equations. This technique is described in [25]. The Stanton number was determined by the formula $\mathrm{St} = q/(\rho_e U_e c_p (T_r - T_w))$, where q is the heat flux, ρ_e and U_e are the density and velocity at the boundary-layer edge, respectively, T_r is the recovery temperature, and c_p is the heat capacity of the gas. The error of determining the Stanton number by this technique was less than 7%.

2. Mathematical Model and Calculation Technique. The mathematical model was formed by Favre-averaged Navier–Stokes equations written in curvilinear coordinates $\eta = \eta(x, r)$, $\xi = \xi(x, r)$:

$$\frac{\partial \boldsymbol{U}}{\partial t} + \frac{\partial \boldsymbol{F}}{\partial \xi} + \frac{\partial \boldsymbol{G}}{\partial \eta} = \frac{\partial \boldsymbol{R}}{\partial \xi} + \frac{\partial \boldsymbol{S}}{\partial \eta} + H_A. \tag{1}$$

Here $\boldsymbol{U} = J(\rho, \rho u, \rho v, E)$ is the vector of conservative variables, ρ is the density, u and v are the velocities in the x and r directions, respectively, E is the total energy per unit volume, and H_A is the source term. The inviscid and viscid fluxes in the cylindrical coordinate system have the form

$$\boldsymbol{F} = J(\tilde{\boldsymbol{F}}\xi_x + \tilde{\boldsymbol{G}}\xi_r), \quad \boldsymbol{G} = J(\tilde{\boldsymbol{F}}\eta_x + \tilde{\boldsymbol{G}}\eta_r), \quad \boldsymbol{R} = J(\tilde{\boldsymbol{R}}\xi_x + \tilde{\boldsymbol{S}}\xi_r), \quad \boldsymbol{S} = J(\tilde{\boldsymbol{R}}\eta_x + \tilde{\boldsymbol{S}}\eta_r),$$

where J is the transformation Jacobian. The vectors of inviscid ($\tilde{\boldsymbol{E}}$ and $\tilde{\boldsymbol{G}}$) and viscid ($\tilde{\boldsymbol{R}}$ and $\tilde{\boldsymbol{S}}$) fluxes are written as follows:

$$\tilde{\boldsymbol{F}} = \begin{pmatrix} \rho u \\ \rho u^2 + p \\ \rho uv \\ (E+p)u \end{pmatrix}, \quad \tilde{\boldsymbol{G}} = \begin{pmatrix} \rho v \\ \rho uv \\ \rho v^2 + p \\ (E+p)v \end{pmatrix},$$

$$\tilde{\boldsymbol{R}} = \begin{pmatrix} 0 \\ t_{xx} \\ t_{xr} \\ ut_{xx} + vt_{xr} - \dot{q}_x \end{pmatrix}, \quad \tilde{\boldsymbol{S}} = \begin{pmatrix} 0 \\ t_{rx} \\ t_{rr} \\ ut_{xr} + vt_{rr} - \dot{q}_r \end{pmatrix}.$$

The total specific energy E includes the internal specific energy e and the kinetic energy of the gas: $E = \rho e + \rho(u^2 + v^2)/2$. The pressure p is calculated by the equation of state for an ideal gas $p = \gamma\rho e$ (γ is the ratio of specific heats). The heat fluxes $\dot{q}_x$ and $\dot{q}_r$ were modeled using the Fourier law.

The source term H_A in Eqs. (1), which allows for problem asymmetry, can be represented as the sum

$$H_A = H_A^{(1)} + H_A^{(2)} + H_A^{(3)},$$

where

$$H_A^{(1)} = -\frac{J}{r}\begin{bmatrix} \rho v \\ \rho uv \\ \rho v^2 + p \\ (i+p)v \end{bmatrix}, \quad H_A^{(2)} = -\frac{J}{r}\begin{bmatrix} 0 \\ t_{xr} \\ t_{rr} - 2\mathrm{M}u^* v/(3r) \\ ut_{xr} + vt_{rr} - \dot{q}_r - 2\mathrm{M}u^* v^2/(3r) \end{bmatrix},$$

$$H_A^{(3)} = \frac{\partial}{\partial\xi}\left[J\xi_x \begin{bmatrix} 0 \\ -2v\mathrm{M}u^*/(3r) \\ 0 \\ -2uv\mathrm{M}u^*/(3r) \end{bmatrix} + J\xi_r \begin{bmatrix} 0 \\ 0 \\ -2v\mathrm{M}u^*/(3r) \\ -2v^2\mathrm{M}u^*/(3r) \end{bmatrix}\right]$$

$$+ \frac{\partial}{\partial\eta}\left[J\eta_x \begin{bmatrix} 0 \\ -2v\mathrm{M}u^*/(3r) \\ 0 \\ -2uv\mathrm{M}u^*/(3r) \end{bmatrix} + J\eta_r \begin{bmatrix} 0 \\ 0 \\ -2v\mathrm{M}u^*/(3r) \\ -2v^2\mathrm{M}u^*/(3r) \end{bmatrix}\right].$$

The stress tensor t_{ij} can be represented as a sum of viscous ($\bar{t}_{ij}$) and Reynolds (τ_{ij}) stresses: $t_{ij} = \bar{t}_{ij} + \tau_{ij}$. In laminar-flow calculations, the turbulent-stress term was assumed to vanish, whereas turbulent and transitional flows were calculated using the Boussinesq hypothesis

$$\tau_{ij} = \mathrm{M}u_\mathrm{t}\Big(\frac{\partial u_i}{\partial x_j} - \frac{\partial u_j}{\partial x_i} - \frac{2}{3}\,\mathrm{div}\,\bar{U}\Big) - \frac{2}{3}\,\rho k\delta_{ij}.$$

To close the averaged equations, we used the two-equation k–ω turbulence model proposed by Wilcox [21]. The turbulent viscosity in the model is calculated by the formula $\mathrm{M}u_\mathrm{t} = \alpha^*\rho k/\omega$, and the turbulent kinetic energy k and specific dissipation of the turbulent kinetic energy to heat ω are determined by the following equations:

$$\begin{aligned} &\frac{\partial\rho k}{\partial t} + \frac{\partial\rho uk}{\partial x} + \frac{\partial\rho vk}{\partial r} = \frac{\partial\alpha_x}{\partial x} + \frac{\partial\alpha_r}{\partial r} - \frac{\rho vk}{r} + \frac{\alpha_r}{r} + P - \beta^*\rho\omega k, \\ &\frac{\partial\rho\omega}{\partial t} + \frac{\partial\rho u\omega}{\partial x} + \frac{\partial\rho v\omega}{\partial r} = \frac{\partial\beta_x}{\partial x} + \frac{\partial\beta_r}{\partial r} - \frac{\rho v\omega}{r} + \frac{\beta_r}{r} + \frac{\alpha\omega}{k}\,P - \beta\rho\omega^2. \end{aligned} \tag{2}$$

Here α_x, α_r, β_x, and β_r are viscous fluxes of turbulent quantities:

$$\alpha_x = \Big(\mathrm{M}u + \frac{\mathrm{M}u_\mathrm{t}}{\sigma_k}\Big)\frac{\partial k}{\partial x}, \quad \alpha_r = \Big(\mathrm{M}u + \frac{\mathrm{M}u_\mathrm{t}}{\sigma_k}\Big)\frac{\partial k}{\partial r}, \quad \beta_x = \Big(\mathrm{M}u + \frac{\mathrm{M}u_\mathrm{t}}{\sigma_\omega}\Big)\frac{\partial\omega}{\partial x}, \quad \beta_r = \Big(\mathrm{M}u + \frac{\mathrm{M}u_\mathrm{t}}{\sigma_\omega}\Big)\frac{\partial\omega}{\partial r};$$

$P = \mathrm{M}u_\mathrm{t}S - 2\rho kD/3$ is the generation of turbulent kinetic energy, where

$$S = 2\Big[\Big(\frac{\partial u}{\partial x}\Big)^2 + \Big(\frac{\partial v}{\partial r}\Big)^2 + \Big(\frac{v}{r}\Big)^2\Big] - \frac{2}{3}\,D^2 + \Big(\frac{\partial v}{\partial x} + \frac{\partial u}{\partial r}\Big)^2, \quad D = \frac{\partial u}{\partial x} + \frac{\partial v}{\partial r} + \frac{v}{r};$$

β, β^*, α, σ_k, and σ_ω are model coefficient, β and β^* are functions of the turbulent Mach number $\mathrm{M}_\mathrm{t} = \sqrt{2k}/a$ ($a = \sqrt{\gamma RT}$ is the local velocity of sound), $\beta^*(\mathrm{M}_\mathrm{t}) = \beta_0^*(1 + \xi^* F(\mathrm{M}_\mathrm{t}))$ and $\beta(\mathrm{M}_\mathrm{t}) = \beta_0 - \beta_0^*\xi^* F(\mathrm{M}_\mathrm{t})$, where

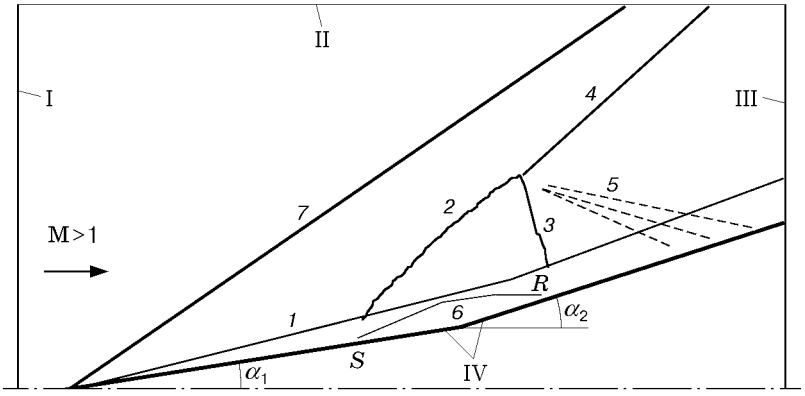

Fig. 2. Flow pattern and computational domain: 1) boundary-layer edge; 2) separation shock; 3) reattachment shock; 4) main shock; 5) expansion fan emanating from the triple point of the λ-configuration; 6) separation region; 7) shock wave emanating from the cone nose; the computational domain boundaries are denoted by I–IV; the separation and reattachment points are indicated by the letters S and R.

$F(\mathrm{M_t}) = (\mathrm{M_t^2} - \mathrm{M_{t0}^2})H(\mathrm{M_t} - \mathrm{M_{t0}})$; $H(x)$ is the Heaviside function. The empirical constants used in the present calculations had the following values: $\alpha^* = 1$, $\alpha = 5/9$, $\beta_0 = 3/40$, $\beta_0^* = 9/100$, $\sigma_k = 1/2$, $\sigma_\omega = 1/2$, $\xi^* = 3/2$, and $\mathrm{M_{t0}} = 1/4$.

The boundary conditions for turbulent parameters on the model surface and external boundary were $\omega \to 6\nu_w/(0.075y^2)$ and $k = 0$ as $y \to 0$ and $\omega \geqslant \omega_e$ and $k \geqslant k_e$ for $y > \delta$ (ν_w is the molecular viscosity on the wall).

Figure 2 shows the flow pattern in the vicinity of the configuration considered. Boundary conditions of different types were set at the computational domain boundaries: input conditions (domain I), simple-wave conditions (domain II), soft boundary conditions (domain III), and no-slip conditions for velocity and adiabaticity or isothermality for temperature (domain IV).

The steady solution of system (1), (2) was determined by the pseudo-transient method on the basis of an implicit four-step finite-difference system of the unified-algorithm type [26] with the use of splitting with regard to physical processes and spatial variables. The Navier–Stokes equations (1) were solved first, and then turbulent quantities were determined from Eqs. (2) for the calculated gas-dynamic parameters. The TVD approach based on the van Leer flux-vector splitting method [27] was used. A detailed description of the numerical algorithm can be found in [28, 29]. This method was previously used for numerical simulation of supersonic turbulent separated flows in the vicinity of plane [30, 31] and axisymmetric [32] configurations. Based on these results, the method offers a good prediction of the parameters of the flows mentioned.

In laminar-flow calculations, the program block designed for calculating turbulent quantities was switched off, and the corresponding value of turbulent viscosity $\mathrm{M}u_\mathrm{t}$ was assumed to be equal to zero. The laminar–turbulent transition was simulated with a fixed position of the transition point, and the transition itself occurred immediately behind the preset point.

3. Results of Calculations and Experiments. Figure 3 shows the experimental flow pattern and calculated density isolines in the boundary-layer separation region, which were obtained under the assumption that the flow within the entire domain is laminar. The calculation reproduces the main elements of the wave pattern of the flow: positions of shock waves and separation-region length. The triple point of the λ-configuration in calculations is further downstream than in the experiment.

To eliminate the influence of numerical (approximation) viscosity, which may turn out to be comparable to molecular (physical) viscosity in laminar-flow calculations, a series of calculations on refined grids was performed. The number of nodes varied within $N = 100$–600 in the x direction and within $M = 50$–400 in the y direction. The experimental and calculated distributions of surface pressure for different grids are compared in Fig. 4 (P_{w1} is the static pressure ahead of the interaction region). The calculation results for $N = 300$, $M = 400$ and $N = 600$, $M = 200$ coincide with the calculation results for $N = 300$, $M = 200$. The calculation reproduces the surface-pressure distribution in the separation region, but the calculated values of P_w behind the reattachment point are slightly overestimated. The calculation does not reveal the experimentally measured decrease in relative pressure behind the reattachment point $x > 130$ mm either.

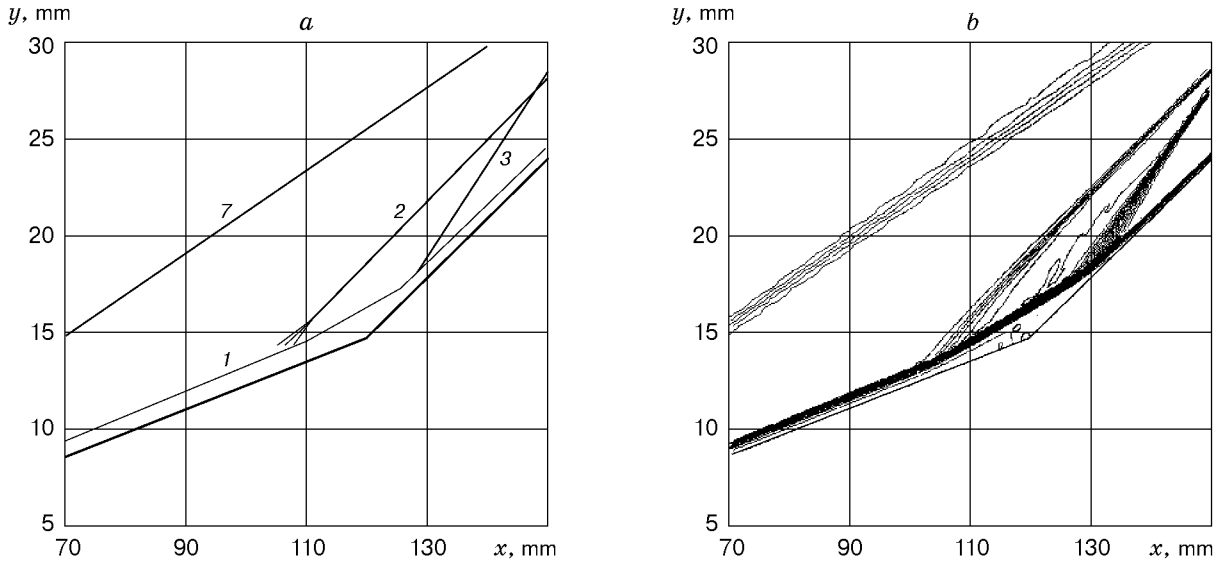

Fig. 3. Experimental flow pattern (a) and calculated density isolines (b) (notation the same as in Fig. 2).

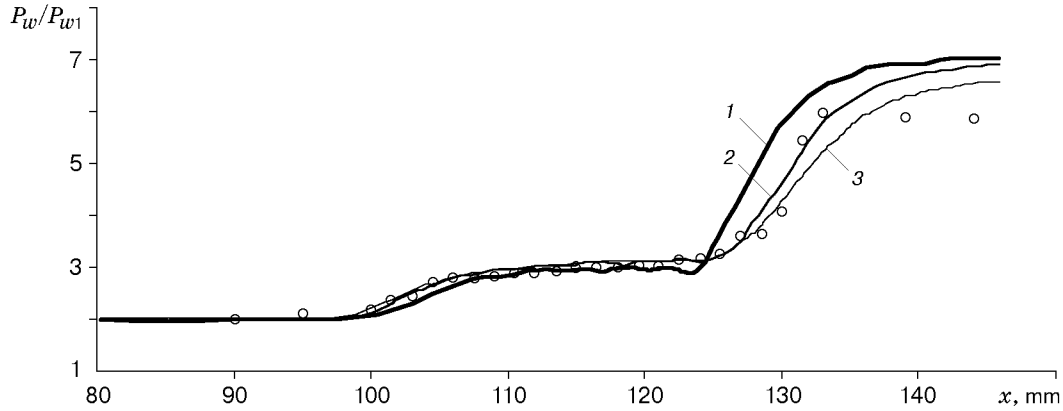

Fig. 4. Pressure distributions obtained in the experiment (points) and calculations on grids with different number of nodes (curves): $N = 100$ and $M = 50$ (1), $N = 150$ and $M = 100$ (2), and $N = 300$ and $M = 200$ (3).

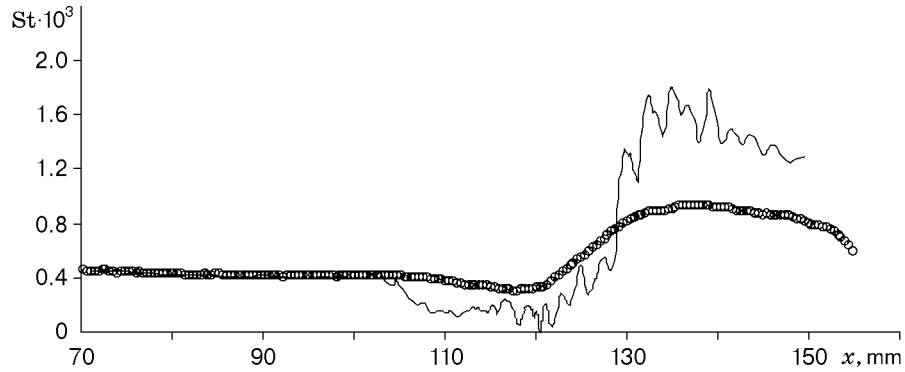

Fig. 5. Calculated (curve) and experimental (points) distributions of the Stanton number along the body.

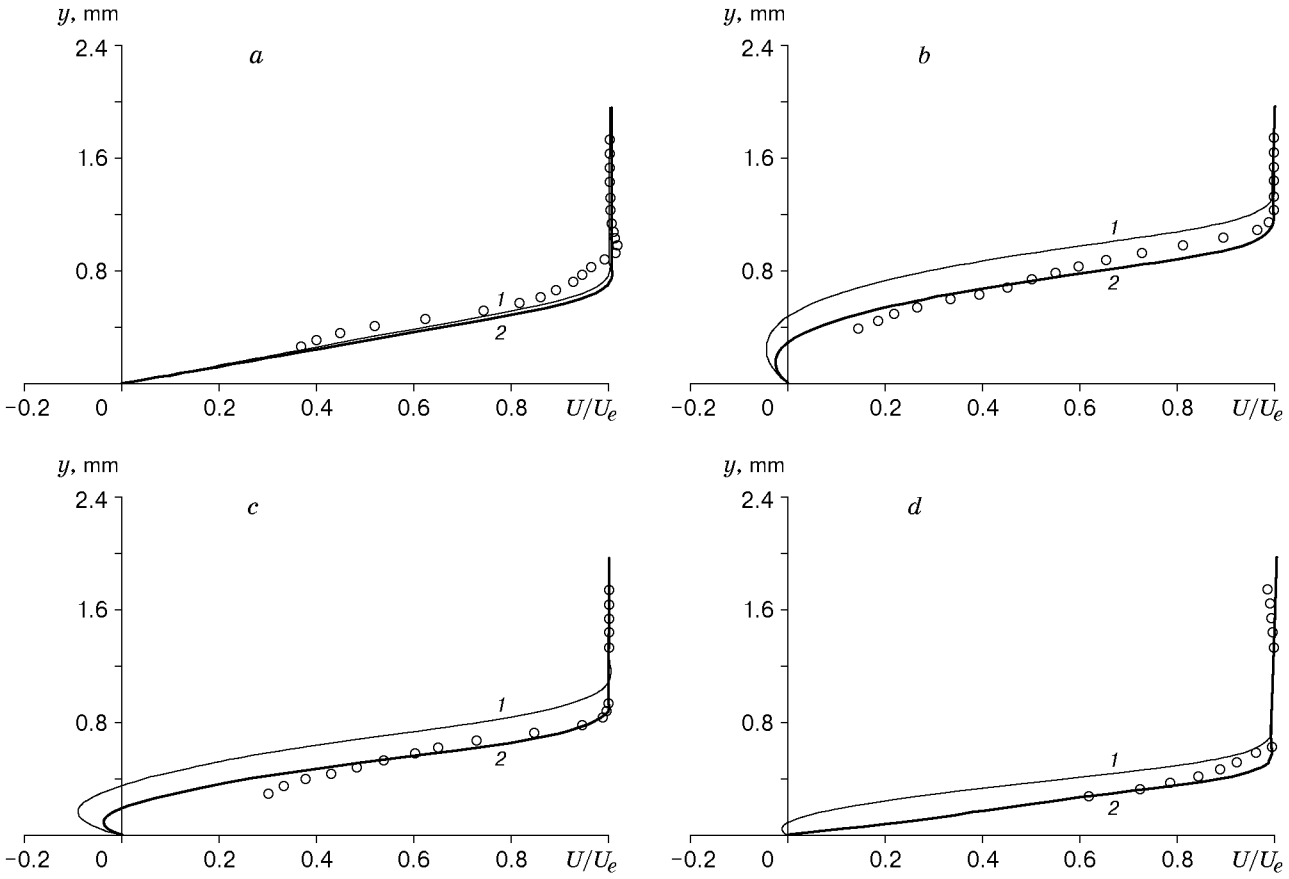

Fig. 6. Experimental (points) and calculated (curves) velocity profiles in various cross sections for the laminar (1) and transitional (2) flow regimes for $x = 90$ (a), 115 (b), 125 (c), and 130 mm (d).

Figure 5 shows the distribution of the Stanton number on the body surface. Good agreement of experimental and calculated data outside the interaction region is noted. The calculated values are lower than the experimental data in the separation region and significantly higher behind the reattachment point. Thus, we may speak about the qualitative agreement only. The discrepancy can be attributed to the use of different methods for determining heat transfer in physical and numerical experiments. In calculations, the condition of a constant temperature (cold wall) was set on the cone surface, and the experimental heat transfer was based on the rate of surface-temperature variation.

Figure 6 shows the calculated and experimental velocity profiles in various cross sections: upstream of the interaction region ($x = 90$ mm), within the separation region ($x = 115$ and 125 mm), and behind the reattachment point ($x = 130$ mm). The calculation overestimates the boundary-layer thickness in the regions of flow separation and reattachment. It was noted in Introduction that a possible reason for this difference may be the transitional or turbulent character of the flow in the separation region. Therefore, calculations with allowance for turbulent viscosity beginning from some fixed cross section were performed. It follows from Fig. 6 that the allowance for the transitional character of the flow permits reaching better agreement between the calculated and experimental velocity profiles.

Parametric calculations performed for different locations of the laminar–turbulent transition show that the transition-point position affects the parameters of the separated flow. Figure 7 shows the pressure distributions for two calculation variants: purely laminar and transitional flow regimes with the transition point at $x = 130$ mm. In the case of the transitional flow, the dependence $P_w(x)$ in the vicinity of the transition point is nonmonotonic. The calculation results are in agreement with the experimentally observed decrease in pressure at $x > 140$ mm. In calculations of transitional regimes, the separation-region length is underestimated. Apparently, the reason is that the reverse near-wall flow "transfers" information from the reattachment point to the separation point, which shifts the separation point downstream. In addition, the allowance for the laminar–turbulent transition in calculations

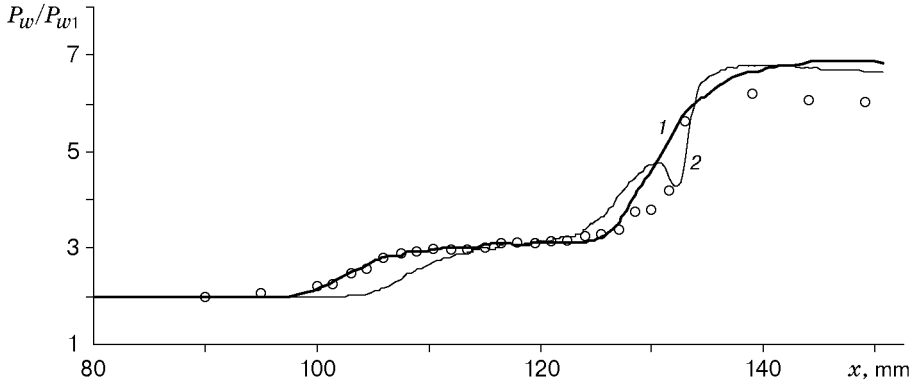

Fig. 7. Experimental (points) and calculated (curves) pressure distributions along the surface for laminar (1) and transitional (2) flow regimes.

by means of sudden "switching" of turbulence at a certain fixed point can be considered as a rough model of the transitional process only. Nevertheless, the parametric calculations performed reproduce the experimental data, which may be considered as a proof of the hypothesis put forward.

4. Conclusions. Experiments and calculations are performed for a supersonic flow in the vicinity of a double cone with angles of 7 and 17° for M = 6. The calculated pressure distribution in the separation region, which was obtained under the assumption of the laminar flow, is in good agreement with the experiment. However, there are some differences in calculated and experimental data on the mixing-layer thickness above the separation region and in pressure distributions behind the reattachment point. To explain these differences, a hypothesis on a possible laminar–turbulent transition in the vicinity of the flow-reattachment point was put forward. The parametric model calculations with allowance for transitional processes yield qualitative reproduction of experimental data.

This work was supported by the Russian Foundation for Fundamental Research (Grant Nos. 00-01-00891 and 02-01-00141).

REFERENCES

1. R. Korkegi, "Survey of viscous interaction associated with high Mach number flight," *AIAA J.*, **9**, 771–784 (1971).
2. J. E. Greene, "Interaction between shock waves and turbulent boundary layers," *Progr. Aerospace Sci.*, **11**, 235–340 (1970).
3. T. C. Adamson (Jr.) and A. F. Messiter, "Analysis of two-dimensional interaction between shock waves and boundary layers," *Annu. Rev. Fluid Mech.*, **12**, 103–138 (1980).
4. D. S. Dolling, "Fifty years of shock wave/boundary layer interaction research — what next?," *AIAA J.*, **39**, No. 8, 1517–1531 (2001).
5. D. D. Knight, "Numerical simulation of compressible turbulent flows using the Reynolds-averaged Navier–Stokes equations," in: *Turbulence in Compressible Flows*, AGARD Report No. 819 (1997), pp. 5-1–5-52.
6. D. R. Chapman, D. M. Kuehn, and H. K. Larson, "Investigation of separated flows in supersonic streams with emphasis on the effect of transition," NACA Report No. 3869, Washington (1957).
7. Paul K. Chang, *Separation of Flows*, Pergamon Press, Oxford (1970).
8. S. A. Gaponov, V. V. Kozlov, A. F. Kurbatskii, and A. A. Maslov, "Hydrodynamic instability and turbulence," *Teplofiz. Aéromekh.*, **4**, No. 2, 225–246 (1997).
9. D. A. Hammond and L. G. Redekopp, "Local and global properties of separation bubbles," *Europ. J. Mech. B Fluids*, **17**, No. 2, 145–164 (1998).
10. M. J. Wright, K. Sinba, J. Olejniczack, and G. V. Candler, "Numerical and experimental investigation of double-cone interaction," *AIAA J.*, **38**, No. 12, 2268–2276 (2000).
11. K. Hozumi, Y. Yamamoto, K. Fujii, et al., "Investigation of hypersonic compression ramp heating at high angles of attack," *J. Spacecraft Rocket*, **38**, No. 4, 488–496 (2001).
12. F. D. Filippis, M. Serpico, and M. Marini, "Comparison between numerical and experimental results on different Hermes elevon shapes," AIAA Paper No. 96-2472, New York (1996).

13. R. P. Nance, T. J. Horvath, and H. A. Hassan, "Transition and turbulence modelling for blunt-body wake flows," AIAA Paper No. 97-2570 (1997).
14. B. R. Hollis and J. N. Perkins, "Transition effects on heating in the wake of blunt body," AIAA Paper No. 97-2569, New York (1997).
15. E. Laurien, "Numerical investigation of laminar-turbulent transition on re-entry capsules," *J. Spacecraft Rocket*, **33**, No. 3, 313–318 (1996).
16. D. Ivanov, A. Obabko, and I. Egorov, "Simulation of separated flows on the base of differential turbulence model, AIAA Paper No. 97-1861, New York (1997).
17. V. A. Bashkin, I. V. Egorov, M. V. Egorova, and D. V. Ivanov, "Evolution of the flowfield structure around a circular cylinder in the presence of laminar–turbulent transition," *Teplofiz. Vys. Temp.*, **38**, No. 5, 759–768 (2000).
18. V. A. Bashkin, I. V. Egorov, M. V. Egorova, and D. V. Ivanov, "Supersonic laminar–turbulent gas flow around a circular cylinder," *Izv. Ross. Akad. Nauk, Mekh. Zhidk. Gaza*, No. 5, 31–43 (2000).
19. B. Edney, "Anomalous heat transfer and pressure distributions on the blunt bodies at hypersonic speeds in the presence of an impinging shock," Report No. 115, Aeronaut. Res. Inst., Stockholm, Sweden (1968).
20. D. F. Robinson, J. E. Harris, and H. A. Hassan, "Unified turbulence closure model for wall bounded and free shear flows," *AIAA J.*, **33**, No. 12, 2325–2331 (1995).
21. D. C. Wilcox, "Turbulence modeling for CFD," DCW Industr. Inc., California, La Caňada (1993).
22. T. J. Coackley and P. G. Huang, "Turbulence modeling for high speed flows," AIAA Paper No. 92-0436, New York (1992).
23. V. D. Grigoriev, G. P. Klemenkov, A. I. Omelaev, and A. M. Kharitonov, "Hypersonic wind tunnel T-326," in: *Aerophysical Research* (collected scientific papers) [in Russian], Inst. Theor. Appl. Mech., Sib. Div., Acad. of Sci. of the USSR, Novosibirsk (1972).
24. A. A. Maslov, A. N. Shiplyuk, A. A. Sidorenko, and Ph. Tran, "Study related to hypersonic boundary layer stability on a cone with a flare," Preprint No. 2-97, Inst. Theor. Appl. Mech., Sib. Div., Russ. Acad. of Sci., Novosibirsk (1997).
25. A. A. Maslov, B. A. Sapogov, and A. N. Shiplyuk, "Technique for heat-flux determination in an aerophysical experiment," *Teplofiz. Aéromekh.*, **3**, No. 2, 157–163 (1996).
26. V. M. Kovenya and N. N. Yanenko, *Method of Splitting in Gas-Dynamic Problems* [in Russian], Nauka, Novosibirsk (1981).
27. B. Van Leer, "Flux-vector splitting for the Euler equations," *Lecture Notes Phys.*, **170**, 507–512 (1982).
28. A. V. Borisov and N. N. Fedorova, "Numerical simulation of turbulent flows near forward-facing steps," *Thermophys. Aeromech.*, **4**, No. 1, 69–83 (1996).
29. I. A. Bedarev and N. N. Fedorova, "Investigation of factors affecting the quality of predicting turbulent separated flows," *Vychisl. Tekhnol.*, **4**, No. 1, 14–32 (1999).
30. I. A. Bedarev, A. V. Borisov, and N. N. Fedorova, "Numerical simulation of the supersonic turbulent separated flows in vicinity of the backward- and forward-faced steps," *Comput. Fluid Dyn. J.*, Spec. number, 194–202 (2001).
31. N. N. Fedorova, I. A. Fedorchenko, and E. Shuelein, "Experimental and numerical study of oblique shock wave/turbulent boundary layer interaction at M = 5," *Comput. Fluid Dyn. J.*, **10**, No. 3, 376–381 (2001).
32. I. A. Bedarev and N. N. Fedorova, "Mathematical modelling of axisymmetric separated flows at super- and hypersonic speeds," in: *Proc. of the 10th Int. Conf. on the Methods of Aerophys. Res.* (Novosibirsk–Tomsk, July 9–16, 2000), Part 3, Publ. House SB RAS, Novosibirsk (2000), pp. 15–20.